Molecular Therapy
Methods & Clinical Development
Original Article

Characterization of AAV-Specific Affinity Ligands: Consequences for Vector Purification and Development Strategies

Mario Mietzsch,[1,3] J. Kennon Smith,[1,3,4] Jennifer C. Yu,[1] Vibhu Banala,[1] Shanan N. Emmanuel,[1] Ariana Jose,[1] Paul Chipman,[1] Nilakshee Bhattacharya,[2,5] Robert McKenna,[1] and Mavis Agbandje-McKenna[1]

[1]Department of Biochemistry and Molecular Biology, Center for Structural Biology, McKnight Brain Institute, College of Medicine, University of Florida, Gainesville, FL, USA; [2]Biological Science Imaging Resource, Department of Biological Sciences, Florida State University, Tallahassee, FL, USA

Affinity-based purification of adeno-associated virus (AAV) vectors has replaced density-based methods for vectors used in clinical settings. This method utilizes camelid single-domain antibodies recognizing AAV capsids. These include AVB Sepharose (AVB) and POROS CaptureSelect affinity ligand for AAV8 (CSAL8) and AAV9 (CSAL9). In this study, we utilized cryo-electron microscopy and 3D image reconstruction to map the binding sites of these affinity ligands on the capsids of several AAV serotypes, including AAV1, AAV2, AAV5, AAV8, and AAV9, representing the range of sequence and structure diversity among AAVs. The AAV-ligand complex structures showed that AVB and CSAL9 bound to the 5-fold capsid region, although in different orientations, and CSAL8 bound to the side of the 3-fold protrusion. The AAV contact residues required for ligand binding, and thus AAV purification, and the ability of the ligands to neutralize infection were analyzed. The data show that only a few residues within the epitopes served to block affinity ligand binding. Neutralization was observed for AAV1 and AAV5 with AVB, for AAV1 with CSAL8, and for AAV9 with CSAL9, associated with regions that overlap with epitopes for neutralizing monoclonal antibodies against these capsids. This information is critical and could be generally applicable in the development of novel AAV vectors amenable to affinity column purification.

INTRODUCTION

Recombinant adeno-associated viruses (rAAVs) are widely used as viral vector systems for therapeutic gene delivery. AAV gene therapy has experienced success in several human clinical trials, including the treatment of hemophilia B with an AAV8 vector expressing therapeutic levels of factor IX protein[1] and of Pompe disease utilizing an AAV1 vector.[2] In addition, three AAV vector biologics have been approved. This includes Glybera (alipogene tiparvovec), an AAV1 vector for the treatment of lipoprotein lipase deficiency by the European Medical Agency (EMA);[3] Luxturna (voretigene neparvovec), an AAV2 vector for the treatment of Leber's congenital amaurosis;[4] and Zolgensma (onasemnogene abeparvovec-xioi), an AAV9 vector for the treatment of spinal muscular atrophy type 1,[5] by the US Food and Drug Administration and EMA. For these and all other AAV-based gene delivery as well as research applications, the efficient production and purification of sufficient vector is essential.

Traditionally, AAVs were purified by gradient ultracentrifugation using cesium chloride,[6] sucrose,[7] or iodixanol.[8] Typically, this required further purification steps such as anion exchange[9] or heparin affinity chromatography columns.[8] In recent years, to expedite AAV purification and to meet good manufacturing practice (GMP) requirements, one-step antibody-based affinity column protocols have become attractive[10] (Figure 1). This includes the use of AVB and the CaptureSelect affinity ligand for AAV8 (CSAL8) and AAV9 (CSAL9), covalently linked to Sepharose and POROS, respectively. These ligands are based on single-chain camelid V_H (heavy chain variable region [VR]) antibodies isolated from non-immunized (AVB) or immunized (CSAL8 and CSAL9) llamas. The AVB column purifies most AAV serotypes with the exception of AAV9 and AAV11,[11] with some serotypes, e.g., AAV8, displaying low purification efficiency.[12] The CSAL8 and CSAL9 products were developed to overcome the shortfalls of AVB, and specifically for purification of AAV8 and AAV9, respectively.

The capsid structures of numerous wild-type AAVs and capsid variants are available.[13–28] The T = 1 icosahedral capsids are composed of 60 viral proteins (VPs) assembled from VP1 (~80 kDa), VP2 (~65 kDa), and VP3 (~60 kDa), in an approximate ratio of 1:1:10,

Received 4 August 2020; accepted 1 October 2020;
https://doi.org/10.1016/j.omtm.2020.10.001.

[3]These authors contributed equally to this work.

[4]Present address: StrideBio, Inc., Research Triangle Park, NC 27709, USA.

[5]Present address: Shared Materials Instrumentation Facility, 101 Science Drive, Duke University, Durham, NC, USA.

Correspondence: Mavis Agbandje-McKenna, Department of Biochemistry and Molecular Biology, Center for Structural Biology, McKnight Brain Institute, College of Medicine, University of Florida, Gainesville, FL, USA.
E-mail: mckenna@ufl.edu

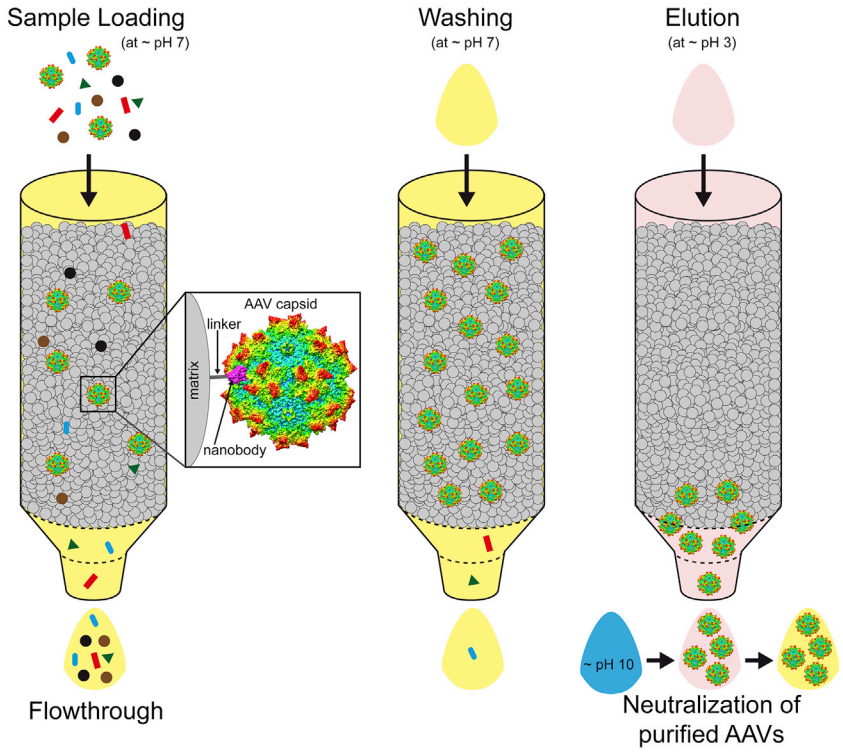

Figure 1. Overview of AAV Purification Using Antibody Affinity Columns

Lysates containing AAV capsids are loaded onto the column at neutral pH. The affinity ligand captures the capsids, while other proteins flow through the column. Column washing at neutral pH further removes non-AAV proteins. AAV capsids are eluted at low pH of pH 2.5–3.0. At this acidic pH, the AAV capsids dissociate from the affinity ligands. The eluted capsids are immediately neutralized with a high pH buffer (~pH 10).

respectively.[29] The VPs consist of a conserved α helix (αA), a βA strand, and an eight-stranded antiparallel β barrel (βB-βI) core motif connected by large loops, named after the β strands that they connect. For example, the HI loop connects the βH and βI strands. These loops form the surface morphology of AAV capsids, including a cylindrical channel at the 5-fold axes, three protrusions surrounding the 3-fold axes, depressions at the 2-fold axes and surrounding the channel at the 5-fold channel, and an elevated region between the 2- and 5-fold axes, termed the 2/5-fold wall. The surface loops display high sequence and structural variability among the AAV serotypes. Nine VRs, VR-I to VR-IX, are defined for the AAVs.[16] These VRs result in structural differences between serotypes and contribute to functional phenotypes, including receptor attachment, tissue tropism, transduction efficiency, and antigenic reactivity.[29,30]

In this study, we compare the purification efficiency of three antibody-based affinity columns, i.e., AVB, CSAL8, and CSAL9, for AAV1, AAV2, AAV5, AAV8, and AAV9, serotypes chosen to represent the range of sequence, structure, and functional diversity among AAVs.[29] The capsid-ligand binding sites were identified by cryo-electron microscopy (cryo-EM) and 3D image reconstruction. These mapped to the 5-fold region for AVB and CSAL9, or to the side of the 3-fold protrusion for CSAL8. The epitopes were confirmed by mutagenesis. Finally, neutralization information for the ligands provided insight into the functional roles of the capsid regions occluded upon binding, rules for improved AAV variant engineering, and guidance for the choice of a purification platform.

RESULTS

AVB and CSAL8 Purify Several AAV Serotypes, whereas CSAL9 Is Specific for AAV9

While AVB has been reported to purify several AAV serotypes,[11,12] to our knowledge, there is no published comparative analysis of the newer affinity resins CSAL8 and CSAL9. The purification efficiencies for AAV1, AAV2, AAV5, AAV8, and AAV9, starting from clarified cell lysates, were compared for AVB, CSAL8, and CSAL9 (Figure 2A). Quantitative PCR (qPCR) quantification of vector titer, in the flowthrough, wash, and elution fractions, showed that AVB effectively purifies AAV1, AAV2, and AAV5, had low efficiency for AAV8, and was unable to purify AAV9 (Figure 2A). CSAL8 efficiently purified AAV1 (and AAV6, data not shown) and AAV8 vectors but was unable to purify AAV2, AAV5, and AAV9 (Figure 2A). CSAL9 specifically purified only AAV9 vectors with high efficiency (Figure 2A). The binding capacities of AVB, CSAL8, and CSAL9 are specified by the manufacturer as $>10^{12}$, $>10^{13}$, and $>10^{14}$ capsids per 1 mL of resin, respectively. While the intention was to determine each resin's ability to purify a given AAV serotype, the yields obtained in the elution fractions were consistent with what is advertised (data not shown). Although the affinity ligands are covalently linked to resins, small quantities of ligand leakage can occur during the purification process (information provided by Thermo Fisher Scientific). The neutralizing potential of the affinity ligands in 100-fold excess per binding site on the capsid, analyzed by a transduction assay, showed AAV1 neutralized by AVB and CSAL8 while CSAL9 had little to no effect (Figure 2B). In contrast, none of the ligands affected AAV2 and AAV8 transduction (Figure 2B), even at lower MOIs as shown for AAV2 (Figure 2C). AAV5 was neutralized by AVB but not CSAL8 or CSAL9, and AAV9 was neutralized only by CSAL9 (Figure 2B).

AVB Binds the 5-Fold Region of AAV Capsids

The binding site of AVB on AAV capsids was determined by cryo-EM and image reconstruction of capsid-ligand complexes. The structures of AAV1:AVB, AAV2:AVB, AAV5:AVB, and AAV8:AVB were reconstructed to 3.9, 9.1, 5.9, and 2.7 Å resolution, respectively. In each structure, five distinct densities of AVB were observed

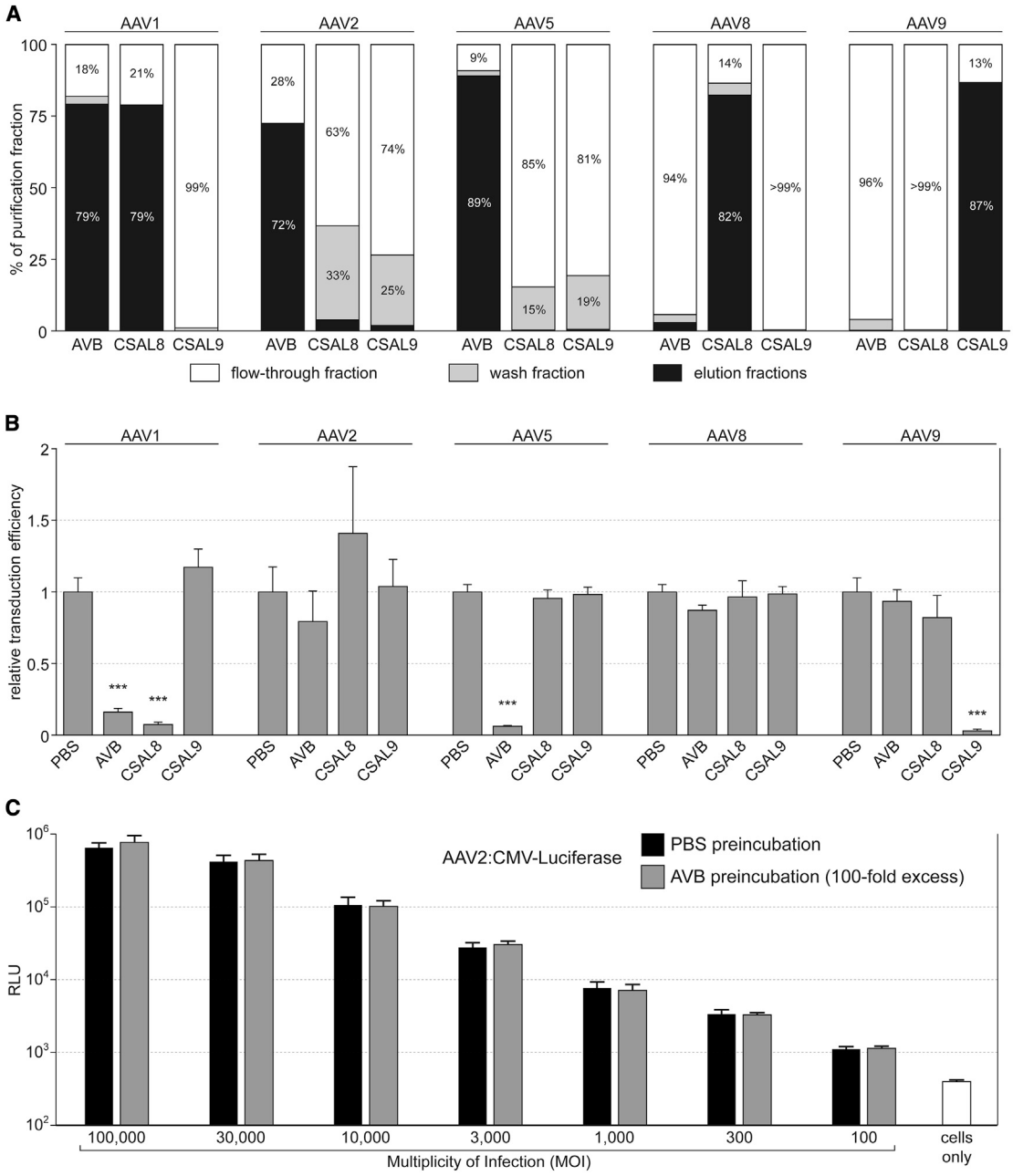

Figure 2. Purification Efficiency and Neutralization Ability of AAV Affinity Ligands

(A) Comparative analysis of AAV purification using AVB, CSAL8, and CSAL9 affinity ligands. Each bar represents an individual AAV purification process. The qPCR titer in each purification fraction is shown as a percentage of the total amount. (B) AAV transduction neutralization assay. HEK293 cells were transduced with rAAV vectors, expressing luciferase, after pre-incubation with PBS, AVB, CSAL8, or CSAL9. The luciferase activity of PBS-treated AAVs was normalized to 1.0. The transduction efficiency of the rAAV-affinity ligand samples are shown as relative thereof. (C) AAV2 transduction assay as in (B) with variable MOIs after pre-incubation with PBS or AVB. The experiments were performed in triplicates and are displayed as mean + SD (n = 3). ***$p < 0.001$.

surrounding the icosahedral 5-fold axis extending toward the 2-5-fold wall and to the base of the 3-fold protrusions (Figures 3A and 3B). The same region of the capsid is occluded by AVB in the four AAV serotypes bound (Figure 3B).

In the absence of the amino acid sequence of AVB, a pseudo-atomic model was used, along with the respective AAV structure, to identify the binding epitopes (Figure 3C). In the high and atomic AAV1 and AAV8:AVB complex structures, respectively, complementarity-

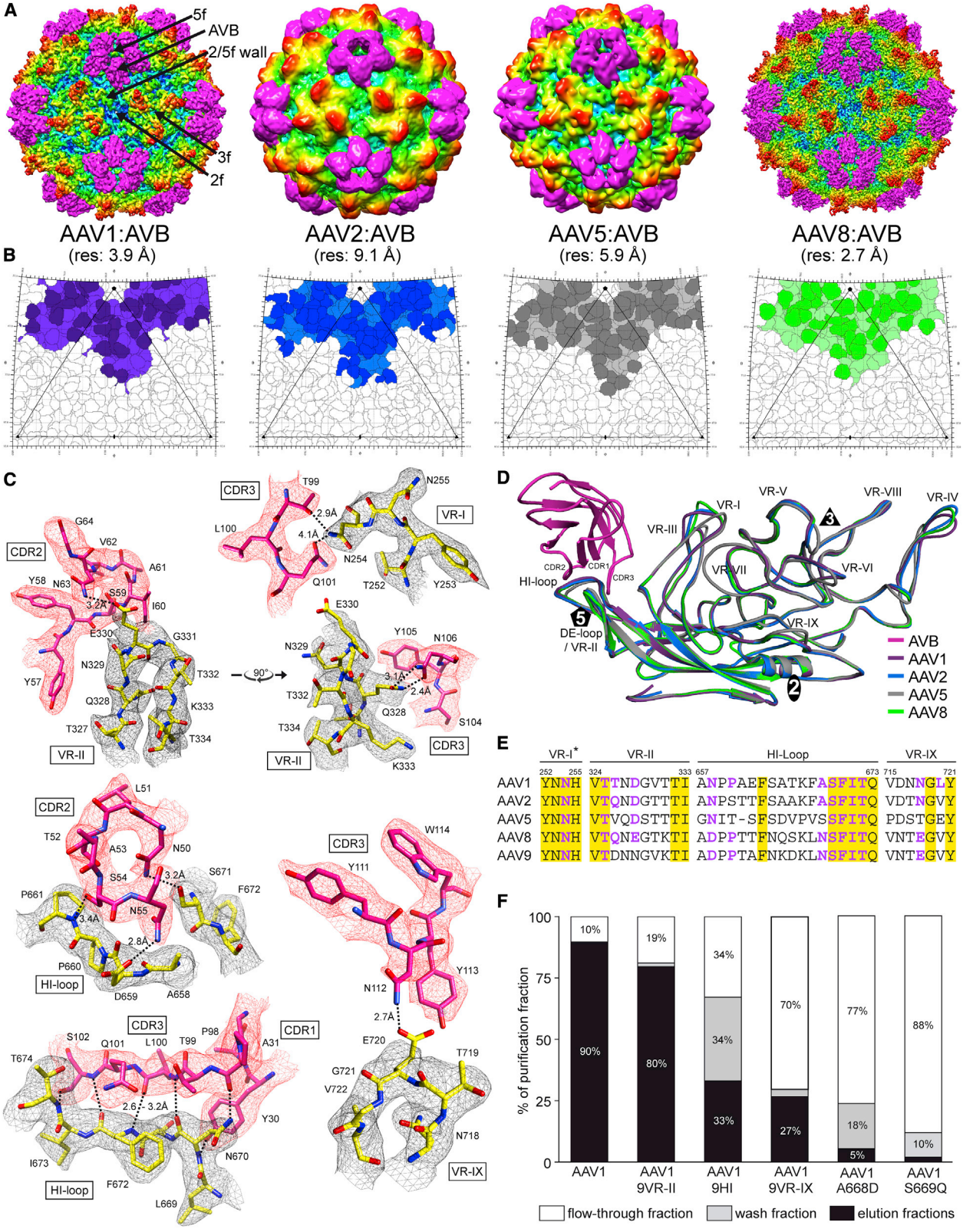

(legend on next page)

determining region (CDR)1 binds to the HI loop and VR-IX, CDR2 to VR-II and the HI loop, and CDR3 to VR-I, VR-II, the HI loop, and VR-IX (Figures 3C, 3D, and S1). The AVB bound similarly in the lower resolution AAV2 and AAV5 structures (Figures 3A, 3B, and 3D) with similar epitopes (Table 1).

Alignment of the amino acids within the AVB epitope identified residues to mutate for confirmation of binding determinants (Figure 3E). Contact amino acids conserved among the five AAV serotypes, e.g., N254 (AAV8 numbering) at the base of VR-I, or those with main-chain contacts, e.g., F672-T674 in the HI loop, were considered to not be determining factors for AVB binding but may play a stabilizing role (Figures 3C and 3E). Residue D328 (VR-II) at the apex of the DE loop is conserved in AAV2 and AAV5, and a glutamic acid in AAV8 (E330) (Figures 3C, 3E, and S1), suggesting that an acidic residue is required for AVB binding, because AAV9 contains an asparagine. However, an AAV9 VR-II substitution into AAV1 (AAV1_9VR-II) did not prevent AVB purification (Figure 3F). VR-IX showed contacts to AVB at N718 and L720 (in AAV1, Figure S1), but neither residue is conserved among the AVB-binding AAVs. Nonetheless, substitution of VR-IX with the corresponding AAV9 sequences reduced the purification efficiency of the resulting AAV variant (AAV1_9VR-IX) (Figure 3F).

The HI loop makes the most extensive contact to AVB with a total of seven residues, including D659, P661, N670, S671, F672, I673, and T674 (AAV8 numbering, Figure 3C). Substitution of the AAV1 HI loop to the corresponding AAV9 sequences reduced the purification efficiency of the resulting AAV variant (AAV1_9HI) (Figure 3F). The contacts on the N-terminal side of the HI loop are likely not critical to AVB binding since the AAV5 HI loop is structurally different in this region compared to the other AAV serotypes due to an amino acid deletion, and yet it still binds AVB (Figures 3E and 3F). The C-terminal end of the HI loop displayed five contacts. However, the AVB density contacts the main chain of residues F672, I673, and T674, and not their side chains (Figures 3C and S1). These amino acids are 100% conserved in the AAVs compared. Similarly, S671 is also 100% conserved but its side chain contacts AVB. Substitution of this residue (S669 in AAV1) with a larger side-chain amino acid (S669Q) prevented purification by AVB (Figure 3F). The other contact is N670 (Figure 3E), which has a larger side chain than the equivalent residues in AAV1, AAV2, and AAV5 (alanine or serine). Thus, the side chain orientation of N670 is changed compared to non-AVB-bound AAV8 structures (Figure S2). Substitution of this residue (AAV1_A668D) reduced purification efficiency significantly (Figure 3F). This observation highlights the importance of the binding epitope information in variant vector development while maintaining purification capability.

CSAL8 Binds the Side of the 3-Fold Protrusions of AAV1 and AAV8 Capsids

The AAV1 and AAV8:CSAL8 complex structures were reconstructed to 3.8 and 2.8 Å resolution, respectively. In both structures, CSAL8 bound to the side of the 3-fold protrusions and the 2/5-fold wall (Figure 4A), occluding a similar region of the capsid (Figure 4B). The fitted CSAL8 pseudo-atomic model showed CDR1 contacting VR-I, CDR2 VR-V and VR-VIII, and CDR3 VR-I, VR-III, VR-V, and VR-VI (Figures 4C–4E and S3). The interactions of one CSAL8 with the capsid involved three symmetry-related VP monomers interacting on the surface. The contacts in VR-I include residues 269–272 (AAV8 numbering), which are located in the structurally conserved portion of the loop, with T270 substituted by a serine in AAV1 (Figure 4E). AAV5 and AAV9 differ in additional residues. Consistently, an AAV9 VR-I loop swap into AAV8 to create AAV8_9VR-I significantly reduced the purification efficiency (by ~55%) of this variant (Figure 4F). However, AAV2 cannot be purified by CSAL8 (Figure 2A) but it is identical to AAV1 in the above range of residues (Figure 4E), suggesting a second binding site to VR-I. The additional contact residues located in VR-III, VR-V, and VR-VI are generally conserved between AAV1, AAV2, and AAV8 except for VR-VIII. Substitution of the AAV8 residues in VR-VIII to AAV2 resulted only in a minor reduction of purification efficiency (Figure 4F), and an AAV2 variant with residues in VR-VIII swapped to AAV1 residues was still unable to be purified with CSAL8 (data not shown). This indicates that VR-VIII plays a minor role in CSAL8 binding. A superposition of the AAV2 and AAV8 capsid structures showed that R471 of AAV2 partially blocks the accessibility of W502 (W505 in AAV8) on the surface of the capsid by CSAL8 (Figure S4). AAV1 and AAV8 possess an alanine or serine in that position. While W505 is not required for CSAL8 binding, substitution of AAV2 residues into AAV8 (AAV8 2:472–475) significantly reduced CSAL8 purification (Figure 4F).

AVB Binds Preferentially to Empty AAV8 Capsids

AAV8 purified by AVB or CSAL8 repeatedly showed a discrepancy in the amount of VP relative to the amount of vector genomes. Concentrated elution fractions subjected to capsid titering by ELISA and

Figure 3. AVB-AAV Capsid Interactions

(A) 3D reconstruction maps of the AAV1:AVB, AAV2:AVB, AAV5:AVB, and AAV8:AVB complexes. The maps, contoured at a sigma (σ) threshold level of 2.0, are radially colored according to distance to the capsid center (blue to red), and the AVB density is in magenta. The icosahedral 2-, 3-, and 5-fold axes, the 2/5-fold wall, and AVB are indicated on the AAV1:AVB capsid map. (B) 2D roadmap projections of the AAV1, AAV2, AAV5, and AAV8 capsids. Regions occluded by AVB are colored, with the model contact residues in a darker shade. (C) AAV8 surface loop models are shown inside their density maps (in black). The amino acid residues are colored C in yellow, O in red, N in blue, and labeled. The AVB model is shown inside a map with atoms colored C in magenta, O in red, and N in blue, with the CDRs labeled. (D) Structural superposition of AAV1, AAV2, AAV5, and AAV8 VP3 ribbon/coil diagrams with the bound AVB shown in magenta. The VRs of the AAVs and the CDRs of AVB are labeled. (E) Amino acid sequence alignment of the AAVs studied in VR-I, VR-II, the HI loop, and VR-IX. The asterisk indicates that this region represents the base of VR-I. Conserved residues are highlighted in yellow, while contact residues in magenta. (F) Analysis of the purification efficiency of AAV1 variants as in Figure 1. (A) and (C) were generated using Chimera,[31] (B) was generated using RIVEM,[32] and (D) was generated using PyMol.[33]

Table 1. Summary of the AAV:Affinity Ligand Complex Data Collections, Reconstruction, and Contact/Occluded Residues on the AAV Capsids

	AAV1: AVB	AAV2: AVB	AAV5: AVB	AAV8: AVB	AAV1: CSAL8	AAV8: CSAL8	AAV9: CSAL9
No. of micrographs	210	79	172	825	156	738	270
Pixel size	1.22	1.85	1.23	1.09	1.22	1.09	1.22
Capsids used for final map	8,106	902	6,188	20,231	20,934	5,764	8,023
Resolution (in Å)	3.89	9.10	5.96	2.74	3.80	2.77	3.58
Contact residues on AAV capsid	254, 325, 326, 328, 657, 659, 668, 670, 671, 672, 718, 720	253, 255, 257, 324, 325, 326, 545, 547, 652, 653, 654, 655, 656, 657, 665, 666, 667, 668, 669, 670, 716, 718	244, 246, 316, 317, 318, 319, 532, 535, 646, 647, 648, 649, 656, 657, 658, 659, 660, 706, 708, 710	255, 328, 330, 659, 661, 670, 671, 672, 673, 674, 720	267, 268, 512, 513, 576, 589	265, 269, 270, 271, 272, 385, 490, 497, 505, 506, 514, 517, 532, 533, 535, 578, 588, 589, 590, 591, 592, 597	329, 330, 332, 659
Occluded residues on AAV capsid	251, 252, 255, 256, 323, 324, 327, 329, 330, 331, 333, 340, 362, 364, 366, 368, 369, 370, 371, 372, 546, 654, 656, 658, 663, 664, 665, 666, 667, 669, 673, 719	250, 254, 320, 321, 322, 323, 327, 328, 329, 331, 338, 362, 363, 364, 366, 367, 368, 369, 370, 663, 664, 671, 672, 714, 717	241, 243, 245, 314, 320, 321, 323, 358, 359, 360, 361, 362, 533, 645, 651, 653, 654, 655, 661	251, 252, 254, 256, 257, 259, 325, 326, 327, 329, 331, 332, 333, 335, 370, 371, 372, 374, 655, 658, 660, 662, 665, 667, 668, 669, 675, 722	262, 269, 270, 271, 272, 381, 382, 383, 384, 385, 470, 472, 485, 488, 495, 510, 513, 514, 515, 528, 529, 531, 533, 534, 575, 583, 584, 586, 588	266, 267, 268, 273, 386, 387, 474, 487, 410, 512, 516, 520, 530, 531, 536, 577, 581, 585, 586	251, 252, 253, 254, 255, 256, 258, 324, 325, 327, 328, 331, 334, 335, 341, 369, 373, 376, 654, 655, 656, 657, 658, 660, 661, 662 663, 667, 669, 670, 671, 672, 673

packaged genome estimation by alkaline gel analysis showed a 3- to 4-fold lower concentration of genomes in AVB-purified AAV8 preparations relative to CSAL8-purified preparations (Figures 5A and 5B). This ratio was supported by qPCR showing on average 4% and 10% full capsids, respectively, in AVB and CSAL8 samples. This observation was confirmed by cryo-EM micrographs in which the genome-containing and empty capsids were counted (Figure 5C). This showed 5% and 18% full capsids, respectively, in AVB-purified and CSAL8-purified samples. This preferential binding of empty capsids by AVB must be considered when purifying wild-type and variant AAV vectors.

CSAL9 Binds the 5-Fold Region of AAV9

The AAV9-CSAL9 complex structure was determined to 3.6 Å resolution. The density map showed CSAL9 decorating the 5-fold axis (Figure 6A), but it adopts a different conformation compared to AVB (Figure 3A). The CDR region of CSAL9 contacts the DE loop while the constant region splays away from the 5-fold axis, unlike AVB, which leans toward it. A 2D roadmap shows CSAL9 binding occluding residues within two virus asymmetric units (Figure 6B), whereas AVB binding occludes residues within the same asymmetric unit (Figure 3B). CSAL9 bound to VR-II and the HI loop with CDR2/3 and CDR1, respectively (Figure 6C and 6D). In VR-II, N329, G330, and K332 contact CSAL9 at a map density threshold of 4 sigma (σ). Compared to the available AAV9 crystal structure[26] the apex of the DE loop shifts 2.8 Å toward CDR2 following CSAL9 binding. The residue combination of N329 and K332 is unique in AAV9, while G330 is conserved in the AAV serotypes compared, with the exception of AAV5, which contains a serine (Figure 6E). Substitution of AAV9 VR-II amino acids into AAV8 (AAV8_9VR-II) allowed partial (23%) purification of the variant (Figures 6E and 6F). In the HI loop, P659 makes contact with CSAL9 at a map density threshold of 2.6σ. However, these residues are conserved in AAV8, a non-binder. In fact, only three amino acids, i.e., A661T, K664Q, and D665S, differ within the HI loop of AAV9 and AAV8, and none of these contacts CSAL9. Nonetheless, substitution of AAV9 HI loop amino acids into AAV8 (AAV8_9HI) conferred a low level (12%) purification of the variant (Figures 6E and 6F). A combination of the AAV9 VR-II and HI loop sequences substituted into AAV8 (AAV8_9VR-II/HI) resulted in a variant with synergistic (65%) improvement of purification efficiency (Figure 6F).

DISCUSSION

An understanding of the AAV capsid-binding interface for purification affinity ligands is important for the development of new engineered AAV variants for gene delivery applications. AVB affinity columns have been commercially available for more than a decade.[10] Previously, a genetic study identified an epitope for AVB within the HI loop of the AAV capsid.[12] This epitope, 663-SPAKFA-668 (AAV3 numbering), is somewhat conserved in AAV1, AAV2, AAV3, AAV6, AAV7, and AAV13, but it is absent in other AAV serotypes also recognized by AVB, e.g., AAV5[34] (Figure 3E). As shown in the current study, only the C-terminal HI loop residues participate in the interaction with AVB, which is validated by the AAV1_A668D and AAV1_S669Q variants that showed reduced purification efficiency (Figure 3F). Consistently, the aspartic acid is present in AAV11, which is unable to be purified by AVB.[11] However, the AVB appears to be a multivalent binder. For example, multiple substitutions in AAV9 compared to AAV1 (Figure 3E) render the capsid unable to be purified by AVB. This would explain the intermediate

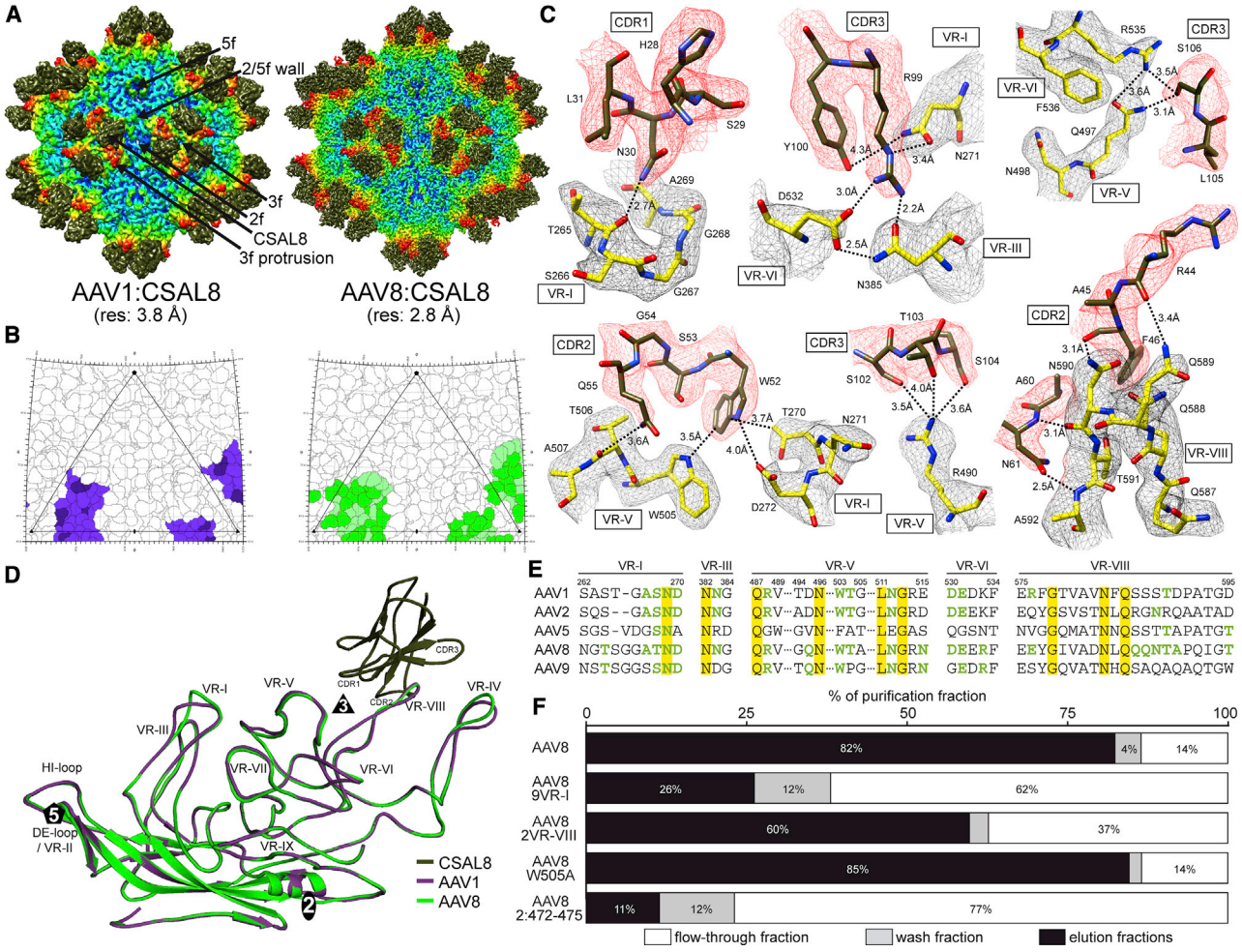

Figure 4. CSAL8-AAV Capsid Interactions

(A) 3D reconstruction maps of the AAV1:CSAL8 and AAV8:CSAL8 complex structures. The maps, contoured at 2.0σ, are radially colored (blue to red) according to distance to the capsid center, and the CSAL8 is in army green. The icosahedral 2-, 3-, and 5-fold axes, the 2/5-fold wall, and CSAL8 are indicated on the AAV1:CSAL8 capsid map. (B) 2D roadmap projections of the AAV1 and AAV8 capsids. Occluded regions are colored with the contact residues indicated in a darker shade. (C) AAV8 surface loop models are shown as in Figure 3. The CSAL8 model is shown inside a red density mesh map with the C in green, O in red, and N in blue. The CDRs are labeled. (D) Structural superposition of AAV1 and AAV8 VP3 with a bound CSAL8 shown as ribbon/coil diagrams. The VRs of the AAVs and the CDRs of CSAL8 are labeled. (E) Amino acid sequence alignment of the AAVs in VR-I, VR-III, VR-V, VR-VI, and VR-VIII. Conserved residues are highlighted in yellow, and contact residues are highlighted in green. (F) Purification efficiency of AAV8 variants as in Figure 1. (A) and (C) were generated using Chimera,[31] (B) was generated using RIVEM,[32] and (D) was generated using PyMol.[33]

binding phenotypes observed for AAV1_9HI and AAV1_9VR-IX and in the previous study (AAV9-SPAKFA).[12]

An interesting observation is the differential neutralization capacity by AVB. While the leakage of ligands during elution from the affinity columns is likely low, neutralization by AVB helps understand the functions of the capsids. In AAV1 and AAV5, both neutralized by AVB, the AVB binding site overlaps with the binding epitope of neutralizing antibodies ADK1b, ADK5a, and ADK5b,[30] respectively. Binding of AVB to the AAV5 capsid likely blocks binding of AAVR to cause neutralization,[35] but not AAV1 since AAVR binds differently in AAV1 capsids.[35] While AVB does not overlap with any known receptor binding site in the AAV1 capsid, it likely occludes an important determinant of AAV1 transduction, including the externalization of VP1u via the 5-fold axis. In contrast to AAV1 and AAV5, AAV2 and AAV8 are not neutralized by AVB, despite having an epitope that also overlaps with some of the residues bound by the AAV2 and AAV8 neutralizing antibodies A20[36] and HL2372,[37] respectively. The A20 antibody is reported to block events associated with genome transcription.[38] AAV2 binds to its receptor heparan sulfate proteoglycan,[39] utilizing amino acids located at the 3-fold protrusion.[40] Thus, AVB binding to the 5-fold region of the AAV2 capsid likely does not interfere with receptor binding. While AVB and HL2372 bind a similar region of the AAV8 capsid, near the 5-fold channel, the HL2372 antibody is significantly larger than the AVB nanobody (150 kDa versus 12 kDa) and could block VP1u externalization

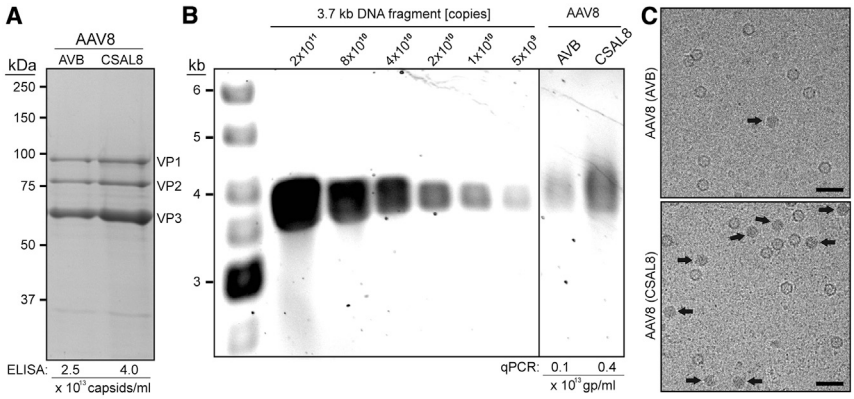

Figure 5. The Empty/Full Ratio of AVB versus CSAL8-Purified rAAV8 Preparations

(A) SDS-PAGE of AVB and CSAL8-purified AAV8. At the bottom is the ELISA quantification of the capsid. (B) Alkaline gel electrophoresis of rAAV8 and control plasmid. Capsid amount loaded is the same for rAAV8 based on the ELISA titer. The size of the packaged vector genome is ~3.9 kb. At the bottom is the qPCR genomic particle (gp) titer. (C) Example of cryo-EM micrographs of the two rAAV8 preparations utilized to count the number of genome-containing (dark) and empty capsid (light appearance). Full capsids are indicated by a black arrow. Scale bars, 50 nm.

during endosomal/lysosomal trafficking or genome uncoating in the nucleus. Thus, it is likely that the region of the capsid masked and sterically hindered by AVB is not the functional determinant(s) blocked by the A20 and HL2372 antibodies.

The CSAL8 and CSAL9 became commercially available recently (https://www.thermofisher.com/us/en/home.html). Unlike AVB, both ligands were developed specifically against AAV8 or AAV9, respectively, with llama immunization. Thus, the binding of CSAL8 by AAV1 (or AAV6) was surprising. While AAV1 and AAV6 differ by only 3 aa on the capsid surface,[22] AAV1 and AAV8 differ by 119 aa, with most differences being located in the surface VR loops.[17] This suggested that only a few residue positions dictate binding by CSAL8. Consistently, substitution of AAV9 VR-1 that differs by 2 aa to the AAV8 VR-1 in variant AAV8_9VR-1 significantly reduced (from 82% to 26%) purification efficiency (Figures 4E and 4F). Binding of CSAL8 to AAV1 blocks the entrance to its sialic acid binding pocket[41] and likely also prevents AAVR binding.[35] Both overlaps could result in the observed neutralization. AAV8 was also reported to be dependent on AAVR for transduction[42] but surprisingly is not neutralized by CSAL8 (Figure 2B). Currently, no glycan receptor has been reported for AAV8, and the exact binding site of the laminin receptor[43] on the AAV8 capsid has not been structurally mapped, but it was proposed to be localized near the 3-fold axis.[17,43] CSAL8 binding to AAV8 would not overlap with the proposed laminin-interacting residues and does not appear to block any functional determinant.

CSAL9 neutralized AAV9 but had no effect on the other four serotypes tested (Figure 2B). The epitope for this ligand, encompassing residues in VR-II and the HI loop (Figure 6), overlaps with that of neutralizing antibody HL2372 mentioned above that was developed to cross-react with AAV8.[44] Interestingly, the CSAL9 binding site is similar to that of AVB with a difference in orientation of the constant region and a more limited footprint (Figures 3 and 6). The CSAL9 epitope does not block the galactose binding site for AAV9, and thus it must be neutralizing via a different mechanism. The binding to the 5-fold channel may be inhibiting VP1u externalization and/or genome uncoating as stated above for AVB with AAV1 and AAV5.

The observed imbalance of capsid and vector genomes from AAV8 preparations purified by AVB versus CSAL8 was not the case for AAV1 (data not shown). This indicates that AVB preferentially binds to a feature on empty AAV8 capsids. However, structural comparison of empty and full AAV8 capsids complexed with AVB or CSAL8 reconstructed to 2.7–2.8 Å resolution did not show major differences on the capsid surfaces explaining the observed binding difference (data not shown). Similar to the recent study on the structures of genome-containing and empty AAV8 capsids,[21] there were differences on the inside of the capsid. Thus, a different factor, possibly the isoelectric point (pI), could serve as the determinant of this differential recognition, a concept discussed previously for separation of empty and genome-containing capsids.[45,46] Such differential binding would explain the low purification efficiency of AAV8 vectors on the AVB column since quantification by qPCR did not account for empty capsids.

New AAV variants are constantly being generated, by rational engineering or directed evolution approaches, to overcome obstacles limiting this gene delivery system, for example, tissue specificity, neutralizing antibodies, or low transduction efficiency. Monoclonal antibodies or nanobodies bind very specific epitopes. Thus, while AAV serotypes share a common capsid morphology, the presence of certain amino acids in certain regions determines whether nanobodies bind. Overall, amino acids are generally more conserved around the 5-fold symmetry axis. Thus, it is not surprising that AVB binds different AAV serotypes at this capsid location. The 3-fold region contains the most sequence and structure variations, and as such it is involved in serotype-specific interactions and is generally not suitable as a site for affinity ligands purifying multiple AAV serotypes. The mapped affinity ligand-binding sites on AAV capsids fulfill an important need in the AAV gene therapy community to garner information enabling the improvement of vector engineering while maintaining purification abilities.

MATERIALS AND METHODS

Cell Culture

HEK293 cells were cultivated as adherent monolayers at 37°C and 5% CO_2 in Dulbecco`s modified Eagle's medium (DMEM) supplemented

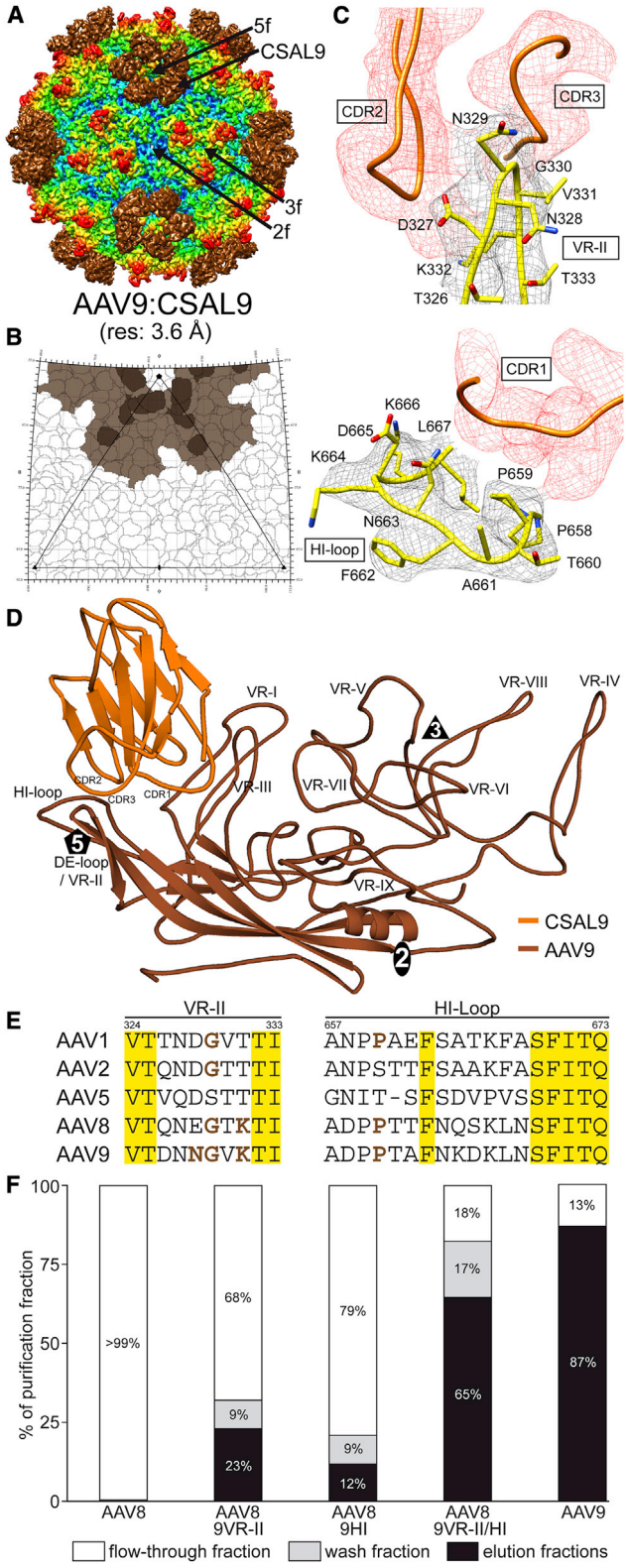

Figure 6. AAV9-CSAL9 Interactions

(A) 3D reconstruction map of the AAV9:CSAL9 complex structure. The map, contoured at 2σ, is radially colored (blue to red) according to distance to the capsid center, and CSAL9 is in brown. The icosahedral 2-, 3-, and 5-fold axes and CSAL9 are indicated. (B) 2D roadmap projection of the AAV9 capsid. Occluded capsid regions are in light brown and contact residues are in dark brown. (C) AAV9 surface loop models are shown as in Figure 3. The CSAL9 model is shown as an orange coil inside a red density mesh and the CDRs are labeled. (D) The ribbon/coil diagram of AAV9 VP3 with a bound CSAL9. The VRs of AAV9 and CDRs of CSAL9 are labeled. (E) Amino acid sequence alignment of the AAVs in VR-II and the HI loop. Conserved residues are highlighted in yellow, and contact residues are in orange. (F) Purification efficiency of AAV8 variants as in Figure 1. (A) and (C) were generated using Chimera[31], B was generated using RIVEM,[32] and D was generated using PyMol.[33]

with 1× antibiotic-antimycotic (Thermo Fisher Scientific, Waltham, MA, USA) and 10% (v/v) fetal bovine serum (Thermo Fisher Scientific). *Sf*9 cells were maintained in suspension culture under constant agitation with serum-free Sf-900 medium supplemented with 1× antibiotic-antimitotic at 27°C.

AAV Production

Vector genome-containing AAVs were produced by triple transfection of HEK293 cells, utilizing pHelper (Stratagene, San Diego, CA, USA), pTR-UF3-luciferase, and either pXR1, pXR2, pXR5, pXR8, or pXR9 as previously described.[47] The transfected cells were harvested 72 h after transfection. Cells were pelleted at 2,000 × *g* for 5 min and resuspended in 1× TD buffer (1× PBS supplemented with 1 mM $MgCl_2$ and 2.5 mM KCl) and subjected to three freeze-thaw cycles. The crude lysates were treated with Benzonase at 37°C for 1 h to degrade unpackaged AAV DNA and centrifuged at 8,000 × *g* for 30 min. AAV vectors released into the culture medium were recovered by addition of 10% polyethylene glycol 8000 (w/v) and subsequent precipitation at 9,000 × *g* for 90 min.

AAV virus-like particles (VLPs) were expressed using a recombinant baculovirus expressing the VPs of the desired AAV serotype. VLPs were purified as described before[48] and dialyzed into 20 mM Tris-HCl and 250 mM NaCl (pH 7.5) for AAV1, AAV2, AAV5, and AAV8, and 20 mM Tris, 350 mM NaCl, and 2 mM $MgCl_2$ (pH 7.4) for AAV9. Virus purity was confirmed by SDS-PAGE and negative stain EM. The AAVs were concentrated using 150-kDa molecular weight cutoff (MWCO) Apollo columns (Orbital Biosciences, Topsfield, MA, USA), and their concentrations were determined using optical density readings at 280 nm with an extinction coefficient of 1.7.

Antibody-Based Affinity Ligand Purification

Prior to AAV purification, the cleared lysates were diluted 1:1 in 1× TD buffer (5.3 mM KCl, 137 mM NaCl, 10 mM Na_2HPO_4, 1.8 mM KH_2PO_4, 1 mM $MgCl_2$). For AVB affinity chromatography, 1-mL prepacked HiTrap AVB Sepharose columns (GE Healthcare, Chicago, IL, USA) were used and attached to a peristaltic pump to load samples and buffers onto the column. For CSAL8 and CSAL9 affinity chromatography, the ~2 mL of resin that contains beads with the covalently-bound nanobodies was added to empty gravity chromatography columns to achieve a 1-mL bed volume. Each affinity

column was equilibrated with 10 column volumes of 1× TD buffer prior to loading of the lysates. The peristaltic pump was set to a flow rate of approximately 0.5 mL/min. Following sample loading, the columns were washed with 20 mL of 1× TD buffer and subsequently eluted with 0.1 M glycine-HCl (pH 2.6). The eluate was immediately neutralized with 1/10 vol of 1 M Tris-HCl (pH 10) (Figure 1).

Quantification of AAV Vectors

Aliquots from the affinity purification process were digested with proteinase K to release the AAV vector genomes from the capsids. To this end, the samples were incubated in buffer containing 10 mM Tris-HCl (pH 8), 10 mM EDTA, and 1% SDS for 2 h at 56°C. The released DNA was purified utilizing the PureLink PCR purification kit (Thermo Fisher Scientific). The copy numbers of vector genome DNAs were determined by qPCR using iQ SYBR Green supermix (Bio-Rad, Hercules, CA, USA). Primers specific for the luciferase gene of the vector genome were used (forward primer, 5′-GCAAAACGCTTCCATCTTCC-3′ and reverse primer, 5′-AGATC CACAACCTTCGCTTC-3′).

AAV Transduction Neutralization Assay

The capacity of the AVB, CSAL8, and CSAL9 affinity ligands to neutralize AAV vectors was analyzed in HEK293 cells seeded in 24-well plates. AAV vectors of the serotypes AAV1, AAV5, AAV8, and AAV9 expressing luciferase were used at an MOI of 100,000, and in the case of AAV2 at a range of different MOIs from 100 to 100,000 were tested. Prior to infection the AAV vectors were pre-incubated for 30 min at 37°C with either AVB, CSAL8, or CSAL9 at a ratio of 100 affinity ligand molecules per binding site on the capsid. 48 h after transduction the luciferase expression was determined by a luciferase assay kit (Promega, Madison, WI, USA) according to the manufacturer's protocol.

Virus Capsid-Affinity Ligand Complex Preparation for Cryo-EM

The purified capsids of AAV1, AAV2, AAV5, AAV8, and AAV9 were mixed with the ~12-kDa nanobodies (provided by Thermo Fisher Scientific) at ratios of 1:600 (capsid/nanobody) to ensure saturated binding. VLPs were mixed with affinity ligands at a ratio of 10 affinity ligand molecules per VP on the capsid. Complexes were incubated for 30 min at 4°C prior to sample vitrification.

Cryo-EM Data Collection

Quantifoil grids with a thin carbon film over the holes were rendered hydrophilic via glow discharge in a Pelco easiGlow for 30 s prior to sampe loading. Virus-ligand complexes were loaded, 3-μL vol each, onto prepared grids and vitrified in liquid ethane by a Vitrobot Mark IV (FEI, Hillsboro, OR, USA) freezing robot. The vitrified grids were then transferred into liquid nitrogen and stored until data collection. Grids were loaded into Gatan 626 cryo-EM sample holders under liquid nitrogen, and placed into an FEI Tecnai F20 electron microscope operating at 200 kV. Data for the AAV2:AVB sample was collected at a magnification of ~50,000 with a 0.5- to 3.0-μm defocus range under low-dose conditions (~20 $e^-/Å^2$) using a Gatan UltraScan 4000 charge-coupled device (CCD) camera at step sizes of ~1.85 Å/pixel. The AAV1:AVB, AAV5:AVB, AAV1:CSAL8, and AAV9:CSAL9 samples were collected at a magnification of ~41,000 with a 0.5- to 4.0-μm defocus range over 50 frames with an accumulated dose of ~60 $e^-/Å^2$ on a Gatan K2 Summit direct electron detector (DED) with corresponding sampling sizes of ~1.22 Å/pixel using either Leginon[49] or the Latitude S software (Gatan, Pleasanton, CA, USA). The AAV8:AVB and AAV8:CSAL8 samples were collected at the Biological Science Imaging Resource of the Florida State University as part of the NIH "Southeastern Center for Microscopy of MacroMolecular Machines (SECM4)" project using the Leginon application[49] on a Titan Krios electron microscope. The microscope was operated at 300 kV and data were collected on a Gatan K3 direct electron detector. During data collection, a total dose of 60 $e^-/Å^2$ was utilized for 50 movie frames per micrograph.

Cryo-EM Image Reconstructions

The datasets collected as movie frames were aligned using MotionCor2 with dose weighting.[50] For 3D image reconstruction, the cisTEM software package was utilized.[51] Briefly, the aligned micrographs were imported into the application and their contrast transfer function (CTF) parameters estimated. This information was used to eliminate micrographs of poor quality. This was followed by automatic particle picking using a particle radius of ~130 Å. This set of particles was subjected to 2D classification to eliminate non-AAV particles (ice and debris) from the automatic picking process. Following the 2D classification, the capsid-complex particles were reconstructed using default settings. This included the *ab initio* 3D model generation, auto refinement, and density map sharpening with a pre-cut-off B factor value of −90 $Å^2$, and variable post-cut-off B factor values such as 0, 20, and 50 $Å^2$. The sharpened density maps were inspected in the Coot and Chimera applications.[31,52] The −90 $Å^2$/0 $Å^2$ sharpened maps were used for assignment of the amino acid main chain and side chains. The resolution of the cryo-reconstructed density maps were estimated based on a Fourier shell correlation (FSC) of 0.143.

Pseudoatomic Modeling and Epitope Prediction

To identify the contact sites of nanobodies on the capsids, the atomic models of AAV1, AAV2, AAV5, AAV8, or AAV9 (PDB: 3GN9, 1LP3, 3NTT, 2QA0, and 3UX1) were fitted into their respective cryo-reconstructed AAV-ligand complex map via rigid-body rotation and translation using the "Fit in map" function of Chimera.[31] For the nanobodies the amino acid sequences are not publicly available. Thus, a generic nanobody structure (PDB: 1MEL) was docked into the density not occupied by the AAV capsids of the highest resolution complex structure for each nanobody. At a resolution of 2.7–2.8 Å the main chain and amino acid side chains were visible, which were used to adjusted the generic nanobody model into the density using Coot.[52] Based on the shape of the side chain density, the amino acids of the model were changed when necessary. The adjusted model of the nanobody was then fitted in the lower resolution complex density maps. At resolutions of 3.6–3.9 Å the main chains of the nanobodies were clearly visible. Contacts in the atomic resolution maps were

defined as distances $\leq$4.0 Å or as continuous density between the AAV capsid and the nanobody at a σ threshold level of 2.0. Visual representations of maps or models were generated using UCSF Chimera[31] or PyMol,[33] respectively.

AAV8 Capsid ELISA

For the quantification of the total concentration of capsids an AAV8 titration ELISA (Progen, Germany) was utilized. All steps were done in triplicate according to the protocol provided by the manufacturer. The colorimetric assay was analyzed by a Synergy HT plate reader (BioTek, Winooski, VT, USA).

Alkaline Gel Electrophoresis

For the alkaline gel electrophoresis, a 0.8% agarose gel in 1× TAE buffer (40 mM Tris, 20 mM acetic acid, and 1 mM EDTA) was utilized. Following solidification, the gel was equilibrated in 1× denaturing buffer (0.5 M NaOH, 50 mM EDTA) for 4 h. Prior to loading, the samples were mixed with denaturing loading dye (final concentration: 1× Ficoll loading buffer, 1× denaturing buffer, 10% SDS). The agarose gel was run at low voltage overnight at 4°C. After the run, the gel was washed and neutralized in 1× TAE buffer for 30 min and subsequently stained in a 0.02% SYBR Gold solution in 1× TAE buffer. The gel was imaged under UV light using a Bio-Rad GelDoc system.

SUPPLEMENTAL INFORMATION

Supplemental Information can be found online at https://doi.org/10.1016/j.omtm.2020.10.001.

AUTHOR CONTRIBUTIONS

M.M. was responsible for AAV purifications and their quantification, cryo-reconstruction, structure analysis and epitope prediction, the transduction analysis of AAVs in the presence of the ligands, and manuscript preparation. J.K.S. was responsible for AAV sample preparation, cryo-EM data collection, as well as cryo-reconstruction, structure analysis, and epitope prediction. J.C.Y. was responsible for AAV purifications and their quantification. V.B. was responsible for cryo-EM data processing. S.N.E. provided AAV9 VLPs and reconstructed the initial AAV9:CSAL9 complex. A.J. was responsible for the quantification of the total capsid titer with the AAV8 ELISA and the quantification of the AAV8 genome titer. P.C. vitrified the samples, screened samples, and collected cryo-EM data. N.B. collected cryo-EM data. R.M. and M.A.-M. were responsible manuscript preparation. M.A.-M. conceived and designed the project. All authors have read and agreed to this version of the manuscript.

CONFLICTS OF INTEREST

M.A.-M. is a consultant for Voyager Therapeutics, Intima Bioscience, and StrideBio, is a Scientific Advisory Board member for AGTC, and has a sponsored research agreement with Voyager Therapeutics, Intima Biosciences, and Adverum Therapeutics. M.A.-M. is also a co-founder of StrideBio. This is a biopharmaceutical company with interest in developing AAV vectors for gene delivery application. The remaining authors declare no competing interests.

ACKNOWLEDGMENTS

The AVB, CSAL8, and CSAL9 affinity ligands were provided by Dr. Pim Hermans of Bac BV, a Thermo Fischer Scientific company. The authors thank the UF-ICBR Electron Microscopy Core for access to electron microscopes utilized for cryo-EM data collection. The TF20 cryo-electron microscopes were provided by the University of Florida College of Medicine (COM) and Division of Sponsored Programs (DSP). The University of Florida COM and NIH GM082946 (to M.A.-M., R.M., and M.M.) provided funds for the research efforts at the University of Florida.

REFERENCES

1. Nathwani, A.C., Tuddenham, E.G., Rangarajan, S., Rosales, C., McIntosh, J., Linch, D.C., Chowdary, P., Riddell, A., Pie, A.J., Harrington, C., et al. (2011). Adenovirus-associated virus vector-mediated gene transfer in hemophilia B. N. Engl. J. Med. *365*, 2357–2365.

2. Smith, B.K., Collins, S.W., Conlon, T.J., Mah, C.S., Lawson, L.A., Martin, A.D., Fuller, D.D., Cleaver, B.D., Clément, N., Phillips, D., et al. (2013). Phase I/II trial of adeno-associated virus-mediated alpha-glucosidase gene therapy to the diaphragm for chronic respiratory failure in Pompe disease: initial safety and ventilatory outcomes. Hum. Gene Ther. *24*, 630–640.

3. Scott, L.J. (2015). Alipogene tiparvovec: a review of its use in adults with familial lipoprotein lipase deficiency. Drugs *75*, 175–182.

4. Lloyd, A., Piglowska, N., Ciulla, T., Pitluck, S., Johnson, S., Buessing, M., and O'Connell, T. (2019). Estimation of impact of RPE65-mediated inherited retinal disease on quality of life and the potential benefits of gene therapy. Br. J. Ophthalmol. *103*, 1610–1614.

5. Al-Zaidy, S.A., and Mendell, J.R. (2019). From clinical trials to clinical practice: practical considerations for gene replacement therapy in SMA type 1. Pediatr. Neurol. *100*, 3–11.

6. Johnson, F.B., Ozer, H.L., and Hoggan, M.D. (1971). Structural proteins of adenovirus-associated virus type 3. J. Virol. *8*, 860–863.

7. Zhou, X., and Muzyczka, N. (1998). In vitro packaging of adeno-associated virus DNA. J. Virol. *72*, 3241–3247.

8. Zolotukhin, S., Byrne, B.J., Mason, E., Zolotukhin, I., Potter, M., Chesnut, K., Summerford, C., Samulski, R.J., and Muzyczka, N. (1999). Recombinant adeno-associated virus purification using novel methods improves infectious titer and yield. Gene Ther. *6*, 973–985.

9. Zolotukhin, S., Potter, M., Zolotukhin, I., Sakai, Y., Loiler, S., Fraites, T.J., Jr., Chiodo, V.A., Phillipsberg, T., Muzyczka, N., Hauswirth, W.W., et al. (2002). Production and purification of serotype 1, 2, and 5 recombinant adeno-associated viral vectors. Methods *28*, 158–167.

10. Smith, R.H., Levy, J.R., and Kotin, R.M. (2009). A simplified baculovirus-AAV expression vector system coupled with one-step affinity purification yields high-titer rAAV stocks from insect cells. Mol. Ther. *17*, 1888–1896.

11. Mietzsch, M., Grasse, S., Zurawski, C., Weger, S., Bennett, A., Agbandje-McKenna, M., Muzyczka, N., Zolotukhin, S., and Heilbronn, R. (2014). OneBac: platform for scalable and high-titer production of adeno-associated virus serotype 1–12 vectors for gene therapy. Hum. Gene Ther. *25*, 212–222.

12. Wang, Q., Lock, M., Prongay, A.J., Alvira, M.R., Petkov, B., and Wilson, J.M. (2015). Identification of an adeno-associated virus binding epitope for AVB sepharose affinity resin. Mol. Ther. Methods Clin. Dev. *2*, 15040.

13. Xie, Q., Bu, W., Bhatia, S., Hare, J., Somasundaram, T., Azzi, A., and Chapman, M.S. (2002). The atomic structure of adeno-associated virus (AAV-2), a vector for human gene therapy. Proc. Natl. Acad. Sci. USA *99*, 10405–10410.

14. Lerch, T.F., Xie, Q., and Chapman, M.S. (2010). The structure of adeno-associated virus serotype 3B (AAV-3B): insights into receptor binding and immune evasion. Virology *403*, 26–36.

15. Govindasamy, L., DiMattia, M.A., Gurda, B.L., Halder, S., McKenna, R., Chiorini, J.A., Muzyczka, N., Zolotukhin, S., and Agbandje-McKenna, M. (2013). Structural insights into adeno-associated virus serotype 5. J. Virol. *87*, 11187–11199.

16. Govindasamy, L., Padron, E., McKenna, R., Muzyczka, N., Kaludov, N., Chiorini, J.A., and Agbandje-McKenna, M. (2006). Structurally mapping the diverse phenotype of adeno-associated virus serotype 4. J. Virol. *80*, 11556–11570.

17. Nam, H.J., Lane, M.D., Padron, E., Gurda, B., McKenna, R., Kohlbrenner, E., Aslanidi, G., Byrne, B., Muzyczka, N., Zolotukhin, S., and Agbandje-McKenna, M. (2007). Structure of adeno-associated virus serotype 8, a gene therapy vector. J. Virol. *81*, 12260–12271.

18. Halder, S., Van Vliet, K., Smith, J.K., Duong, T.T., McKenna, R., Wilson, J.M., and Agbandje-McKenna, M. (2015). Structure of neurotropic adeno-associated virus AAVrh.8. J. Struct. Biol. *192*, 21–36.

19. Mikals, K., Nam, H.J., Van Vliet, K., Vandenberghe, L.H., Mays, L.E., McKenna, R., Wilson, J.M., and Agbandje-McKenna, M. (2014). The structure of AAVrh32.33, a novel gene delivery vector. J. Struct. Biol. *186*, 308–317.

20. Burg, M., Rosebrough, C., Drouin, L.M., Bennett, A., Mietzsch, M., Chipman, P., McKenna, R., Sousa, D., Potter, M., Byrne, B., et al. (2018). Atomic structure of a rationally engineered gene delivery vector, AAV2.5. J. Struct. Biol. *203*, 236–241.

21. Mietzsch, M., Barnes, C., Hull, J.A., Chipman, P., Xie, J., Bhattacharya, N., Sousa, D., McKenna, R., Gao, G., and Agbandje-McKenna, M. (2020). Comparative analysis of the capsid structures of AAVrh.10, AAVrh.39, and AAV8. J. Virol. *94*, e01769-19.

22. Ng, R., Govindasamy, L., Gurda, B.L., McKenna, R., Kozyreva, O.G., Samulski, R.J., Parent, K.N., Baker, T.S., and Agbandje-McKenna, M. (2010). Structural characterization of the dual glycan binding adeno-associated virus serotype 6. J. Virol. *84*, 12945–12957.

23. Drouin, L.M., Lins, B., Janssen, M., Bennett, A., Chipman, P., McKenna, R., Chen, W., Muzyczka, N., Cardone, G., Baker, T.S., and Agbandje-McKenna, M. (2016). Cryo-electron microscopy reconstruction and stability studies of the wild type and the R432A variant of adeno-associated virus type 2 reveal that capsid structural stability is a major factor in genome packaging. J. Virol. *90*, 8542–8551.

24. Tan, Y.Z., Aiyer, S., Mietzsch, M., Hull, J.A., McKenna, R., Grieger, J., Samulski, R.J., Baker, T.S., Agbandje-McKenna, M., and Lyumkis, D. (2018). Sub-2 Å Ewald curvature corrected structure of an AAV2 capsid variant. Nat. Commun. *9*, 3628.

25. Bennett, A., Keravala, A., Makal, V., Kurian, J., Belbellaa, B., Aeran, R., Tseng, Y.S., Sousa, D., Spear, J., Gasmi, M., and Agbandje-McKenna, M. (2020). Structure comparison of the chimeric AAV2.7m8 vector with parental AAV2. J. Struct. Biol. *209*, 107433.

26. DiMattia, M.A., Nam, H.J., Van Vliet, K., Mitchell, M., Bennett, A., Gurda, B.L., McKenna, R., Olson, N.H., Sinkovits, R.S., Potter, M., et al. (2012). Structural insight into the unique properties of adeno-associated virus serotype 9. J. Virol. *86*, 6947–6958.

27. Kaelber, J.T., Yost, S.A., Webber, K.A., Firlar, E., Liu, Y., Danos, O., and Mercer, A.C. (2020). Structure of the AAVhu.37 capsid by cryoelectron microscopy. Acta Crystallogr. F Struct. Biol. Commun. *76*, 58–64.

28. Guenther, C.M., Brun, M.J., Bennett, A.D., Ho, M.L., Chen, W., Zhu, B., Lam, M., Yamagami, M., Kwon, S., Bhattacharya, N., et al. (2019). Protease-activatable adeno-associated virus vector for gene delivery to damaged heart tissue. Mol. Ther. *27*, 611–622.

29. Mietzsch, M., Pénzes, J.J., and Agbandje-McKenna, M. (2019). Twenty-five years of structural parvovirology. Viruses *11*, 362.

30. Emmanuel, S.N., Mietzsch, M., Tseng, Y.S., Smith, J.K., and Agbandje-McKenna, M. (2020). Parvovirus capsid-antibody complex structures reveal conservation of antigenic epitopes across the family. Viral Immunol. Published online April 21, 2020. https://doi.org/10.1089/vim.2020.0022.

31. Pettersen, E.F., Goddard, T.D., Huang, C.C., Couch, G.S., Greenblatt, D.M., Meng, E.C., and Ferrin, T.E. (2004). UCSF Chimera—a visualization system for exploratory research and analysis. J. Comput. Chem. *25*, 1605–1612.

32. Xiao, C., and Rossmann, M.G. (2007). Interpretation of electron density with stereographic roadmap projections. J. Struct. Biol. *158*, 182–187.

33. DeLano, W.L. (2002). The PyMOL Molecular Graphics System (DeLano Scientific).

34. Mietzsch, M., Casteleyn, V., Weger, S., Zolotukhin, S., and Heilbronn, R. (2015). OneBac 2.0: Sf9 cell lines for production of AAV5 vectors with enhanced infectivity and minimal encapsidation of foreign DNA. Hum. Gene Ther. *26*, 688–697.

35. Zhang, R., Xu, G., Cao, L., Sun, Z., He, Y., Cui, M., Sun, Y., Li, S., Li, H., Qin, L., et al. (2019). Divergent engagements between adeno-associated viruses with their cellular receptor AAVR. Nat. Commun. *10*, 3760.

36. McCraw, D.M., O'Donnell, J.K., Taylor, K.A., Stagg, S.M., and Chapman, M.S. (2012). Structure of adeno-associated virus-2 in complex with neutralizing monoclonal antibody A20. Virology *431*, 40–49.

37. Havlik, L.P., Simon, K.E., Smith, J.K., Klinc, K.A., Tse, L.V., Oh, D.K., Fanous, M., Meganck, R.M., Mietzsch, M., Agbandje-McKenna, M., et al. (2020). Co-evolution of AAV capsid antigenicity and tropism through a structure-guided approach. J. Virol. *94*, e00976-20.

38. Aydemir, F., Salganik, M., Resztak, J., Singh, J., Bennett, A., Agbandje-McKenna, M., and Muzyczka, N. (2016). Mutants at the 2-fold interface of adeno-associated virus type 2 (AAV2) structural proteins suggest a role in viral transcription for AAV capsids. J. Virol. *90*, 7196–7204.

39. Summerford, C., and Samulski, R.J. (1998). Membrane-associated heparan sulfate proteoglycan is a receptor for adeno-associated virus type 2 virions. J. Virol. *72*, 1438–1445.

40. O'Donnell, J., Taylor, K.A., and Chapman, M.S. (2009). Adeno-associated virus-2 and its primary cellular receptor—cryo-EM structure of a heparin complex. Virology *385*, 434–443.

41. Huang, L.Y., Patel, A., Ng, R., Miller, E.B., Halder, S., McKenna, R., Asokan, A., and Agbandje-McKenna, M. (2016). Characterization of the adeno-associated virus 1 and 6 sialic acid binding site. J. Virol. *90*, 5219–5230.

42. Pillay, S., Meyer, N.L., Puschnik, A.S., Davulcu, O., Diep, J., Ishikawa, Y., Jae, L.T., Wosen, J.E., Nagamine, C.M., Chapman, M.S., and Carette, J.E. (2016). An essential receptor for adeno-associated virus infection. Nature *530*, 108–112.

43. Akache, B., Grimm, D., Pandey, K., Yant, S.R., Xu, H., and Kay, M.A. (2006). The 37/67-kilodalton laminin receptor is a receptor for adeno-associated virus serotypes 8, 2, 3, and 9. J. Virol. *80*, 9831–9836.

44. Tseng, Y.S., Vliet, K.V., Rao, L., McKenna, R., Byrne, B.J., Asokan, A., and Agbandje-McKenna, M. (2016). Generation and characterization of anti-adeno-associated virus serotype 8 (AAV8) and anti-AAV9 monoclonal antibodies. J. Virol. Methods *236*, 105–110.

45. Qu, W., Wang, M., Wu, Y., and Xu, R. (2015). Scalable downstream strategies for purification of recombinant adeno-associated virus vectors in light of the properties. Curr. Pharm. Biotechnol. *16*, 684–695.

46. Wang, C., Mulagapati, S.H.R., Chen, Z., Du, J., Zhao, X., Xi, G., Chen, L., Linke, T., Gao, C., Schmelzer, A.E., and Liu, D. (2019). Developing an anion exchange chromatography assay for determining empty and full capsid contents in AAV6.2. Mol. Ther. Methods Clin. Dev. *15*, 257–263.

47. Jose, A., Mietzsch, M., Smith, J.K., Kurian, J., Chipman, P., McKenna, R., Chiorini, J., and Agbandje-McKenna, M. (2018). High-resolution structural characterization of a new adeno-associated virus serotype 5 antibody epitope toward engineering antibody-resistant recombinant gene delivery vectors. J. Virol. *93*, e01394-18.

48. Bennett, A.D., Wong, K., Lewis, J., Tseng, Y.S., Smith, J.K., Chipman, P., McKenna, R., Samulski, R.J., Kleinschmidt, J., and Agbandje-McKenna, M. (2018). AAV6 K531 serves a dual function in selective receptor and antibody ADK6 recognition. Virology *518*, 369–376.

49. Suloway, C., Pulokas, J., Fellmann, D., Cheng, A., Guerra, F., Quispe, J., Stagg, S., Potter, C.S., and Carragher, B. (2005). Automated molecular microscopy: the new Leginon system. J. Struct. Biol. *151*, 41–60.

50. Zheng, S.Q., Palovcak, E., Armache, J.P., Verba, K.A., Cheng, Y., and Agard, D.A. (2017). MotionCor2: anisotropic correction of beam-induced motion for improved cryo-electron microscopy. Nat. Methods *14*, 331–332.

51. Grant, T., Rohou, A., and Grigorieff, N. (2018). *cis*TEM, user-friendly software for single-particle image processing. eLife *7*, e35383.

52. Emsley, P., and Cowtan, K. (2004). Coot: model-building tools for molecular graphics. Acta Crystallogr. D Biol. Crystallogr. *60*, 2126–2132.